A phase-field method coupled with CALPHAD for the simulation of ordered κ-carbide precipitates in both disordered γ and α phases in low density steel

Rahnama, A, Dashwood, R & Sridhar, S

A phase-field method coupled with CALPHAD for the simulation of ordered κ-carbide precipitates in both disordred γ and α phases in low density steel

Aireza Rahnama, Richard Dashwood, Sridhar Seetharaman[1]

International Digital Laboratory, Warwick Manufacturing Group, University of Warwick, Coventry, United Kingdom, CV4 7AL

Abstract

In order to simulate multi-component diffusion controlled precipitation of ordered phases in low density steels using the phase-field method, the Gibbs free energy of the γ, α and κ phases in the quaternary Fe-Mn-Al-C system was linked to the CALPHAD method using a three-sublattice model which is based on the accumulation of considerable thermodynamic data in multi-component systems and the assurance of continuous variation of the interface area. This model includes the coherent precipitation of κ phase from a disordered FCC γ phase and semi-coherent precipitation of the same κ phase from a disordered BCC α structure. The microstructure evolution of κ-carbide was simulated with three-dimensional phase-field model. The simulation was first performed for a single particle in both γ and α phases to investigate the evolution of interfacial and elastic strain energy during the precipitation process. The simulation results show that κ has a cuboidal morphology in γ and elongated plate-like morphology in α which is in agreement with the morphologies reported in the literature. The multi-particle simulations were also performed for the precipitation of κ phase from both disordered γ and α. The results also demonstrate that the size of κ precipitates in γ is remarkably smaller than that in α phase.

Keywords: Phase-field, Low Density Steel, κ-carbide, CALPHAD

2010 MSC: 00-01, 99-00

☆Fully documented templates are available in the elsarticle package on CTAN.

1. Introduction

The weight reduction of automotive vehicles has been stimulated by improvements through reduction in vehicles' exhaust emission and minimization of fuel consumption. [1, 2]. The development of lightweight steels is recognized as a possible measure [3, 4] to achieve these goals. The low density steels with superior combinations of specific strength and ductility have attracted considerable attention recently [5, 6, 7]. It was reported that the addition of 5-6 wt.% of Al results in 8-10% weight saving compared to conventional automotive steels [8]. Various alloys based on the Fe-Mn-Al-C system have been developed. The strengthening mechanisms for these low density steels include precipitation hardenable (α+κ-carbide) [10], duplex phase (α+γ) [11, 12], or triplex phase (α+γ+κ-carbides) types [8, 7]. Many scholars have been investigating the effect of $(Fe, Mn)_3AlC$ perovskite κ-carbide as the most effective strengthening mechanism of austenite [13, 14, 18], since the austenite phase has the characteristics of low yield strength. The nano-sized, ordered κ precipitates are reported to increase the yield strength and tensile strength above 1 GPa [14]. Therefore, the utilization of austenite and κ precipitates is normally considered as a promising approach for improvement of mechanical properties in low density steels.

Many researchers have attempted to simulate microstructure evolution using various computational methods [15, 16, 17]. However, phase-field has been considered as the most powerful method for predicting the mesoscale morphological and microstructure evolution [19, 20, 22]. Phase field modelling is a phenomenological approach. Thus, the input parameters play a key role in obtaining realistic results. The bulk free energies of each phase as a function of all the variables included in the model are determined by the parametrization of phase-field models. Phase field methods coupled with CALPHAD databases is, thus, one of the best approach to investigate the complex morphological developments in multicomponent alloys. To provide a realistic thermodynamic parametrization of all phases in a material, Grafe et al. [23] proposed to employ thermodynamic data from databases based on the CALPHAD method. This approach has been recently employed for various studies [24, 37].

Although many studies have been devoted to simulate the precipitation of ordered

2

phases[26, 27, 28, 37, 57], there is no single phase field model has been developed to simulate the precipitation kinetics and microstructural evolution of κ-carbide in a quaternary system like Fe-Mn-Al-C. In this study, an effort was made to simulate the precipitation of ordered κ-carbide from both disordered FCC and BCC phases. The Gibbs free energy for multi-component Fe-Mn-Al-C systems was linked to CALPHAD method. A Gibbs energy single formalism for κ/γ and κ/α phases with a three-sublattice model for this quaternary system was employed. In these simulations, the order parameter of each element correspond to long-range ordering in the κ phase, because the order parameter is expressed using the element site fractions of a three-sublattice model in the CALPHAD method. This approach is based on report for ordering mechanism in Ni-Al system [37]. The simulation results illustrating the effects of ordering, elastic strain and interfacial energy on the precipitation evolution.

2. Model

To control the materials properties, it is important to understand the microstructural development. Experimental studies on phase equilibria have been, thus, carried out for the Fe-Al-C [33] and Fe-Mn-Al-C [34] systems. Furthermore, CALPHAD type thermodynamic calculations have been extensively performed in materials science to critically assess the phase relations under arbitrary thermodynamic conditions, for instance investigation of the Fe-Al-C system has been done by Ohtani et al. [35] and Connetable et al. [48] where the ordered κ-carbide in the Fe-Al-C ternary system was calculated by applying formalisms that allow intermixing between Fe and Al, and non-stoichiometry in the carbon content. However, a narrow range of Al content were calculated in both studies. In addition, the carbon content region in the Fe-Al-C system clearly deviates toward the low carbon content from the stoichiometric composition Fe_3AlC [33] whereas this is not the case in the Mn-Al-C system where carbon content exactly reaches the stoichiometric composition Mn_3AlC [36]. Chin et al. [53] extended the thermodynamic database for the ternary Fa-Al-C system to the quaternary Fe-Mn-Al-C system.

In this study, an ordinary two-sublattice CALPHAD type model for the excess en-

3

ergy term were used for the Gibbs energy of the disordered phases FCC (γ) or BCC (α) solution [42, 43]. Also, a three-sublattice model was employed, $(Fe, Mn)_3 Al_2 (C, Va)_1$, which enables intermixing between Fe and substitutional Mn atoms on the face site while allows incomplete occupation of C atoms in the central octahedral site of the ordered κ-phase [53].

The sum molar Gibbs energy for the disordered FCC (γ) or BCC (α) phases was expressed as:

$$G^{disord} = \sum_i c_i G_i^{disord} + RT \sum_i c_i ln c_i +$$
$$\sum_i \sum_{j>i} c_i c_j \sum_{n=0}^{m} (^n L_{i:j}^{disord} (c_i - c_j)^n) +$$
$$\sum_i \sum_{j>i} \sum_{k>j} c_i c_j c_k L_{i,j:k}^{disord} \quad (1)$$

For each alloying element, the site fraction 'i' on each sublattice 's' is referred by $y_i^{(s)}$, where i, j, k and l can be Mn, Al, or C on any of the sublattices. c_i denotes a mole fraction of element 'i', R and T are the gas constant and temperature. G_i^{disord} refers to a molar Gibbs energy of element 'i' with the structure of FCC or BCC. $^n L_{i,j}^{disord}$ and L_i^{disord}, j, k denote binary and ternary interaction parameters, respectively. For κ phase, the molar Gibbs energy can be described as the sum of an ordering contribution of the κ-carbide phase and the Gibbs energy of the diordered γ or α phases [37]:

$$G(c_i, y^{(s)_i}) = G^{disord}(c_i) + \Delta G^{ord}$$
$$= [\sum_i c_i G_i^{disord} + RT \sum_i c_i ln c_i +$$
$$\sum_i \sum_{j>i} c_i c_j \sum_{n=0}^{m} (^n L_{i:j}^{disord} (c_i - c_j)^n) +$$
$$\sum_i \sum_{j>i} \sum_{k>j} c_i c_j c_k L_{i,j:k}^{disord}] + \Delta G^{ord}(y_i^{(s)}) \quad (2)$$

4

$\Delta G^{ord}(y_i^{(s)})$ is written as:

$$\Delta G^{ord}(y_i^{(s)}) = \Delta G^{L'1_2}(y_i^{(s)}) - \Delta G^{L1_2}(y_i^{(s)} = c_i) \qquad (3)$$

The term $\Delta G^{L'1_2}(y_i^{(s)})$ is described as:

$$\Delta G^{L'1_2}(y_i^{(s)}) = \sum_i \sum_j \sum_k y_i^{(1)} y_j^{(2)} y_k^{(3)} \Delta G_{i:j:k}^{L'1_2} +$$
$$\frac{RT}{4} \sum_s \sum_i y_i^{(s)} ln(y_i^{(s)})$$
$$+ \sum_s \sum_i \sum_{j>i} y_i^{(s)} y_j^{(s)} \sum_{n=0}^1 ({}^n L_{i:j}^{L'1_2}(y_i^{(s)} - y_j^{(s)})) \qquad (4)$$

In Eq.3, the two terms cancel each other when the site fractions are equal, thus corresponding to a disordered phase. These two terms are calculated using the same function in the sublattice formalism but different site fractions. $\Delta G^{ord}(y_i^{(s)})$ is function of the site fraction $y_i^{(s)}$ and $\Delta G^{L'1_2}(y_i^{(s)} = c_i)$ of the site fractions of the disorder phase of same composition. It should be noted that this formalism was proposed by Dupin et al. after classical sublattice formalism and incorporated into ThermoCalc by Sundman [50]. In the current work, we followed they formalism where we introduced the relationship between overall composition x_i and site fractions $y_i^{(s)}$ as $dx_i = \frac{3}{4} dy_i^{(I)} + \frac{1}{4} dy_i^3$. All variables in Eq.1, Eq.2, and Eq.3 can be assessed by phase diagram calculations as listed in Table.1.

5

Table 1: Thermodynamic parameters for the Fe-Mn-Al-C quaternary system.

$BCC : (Fe, Mn, Al)_1(C, Va)_3$	
$^0G_{Al:C}^{BCC} =^0 G_{Al}^{FCC} + 3^0G_C^{graphite} + 100000 + 80T$	[48]
$L_{Al:C,Va}^{BCC} = 130000 + 14T$	[48]
$L_{Fe:C,Va}^{BCC} = -190T$	[42]
$L_{Al,Fe:Va}^{BCC} = -122960 + 31.9888T + (y_{Al} - y_{Fe})2945.2$	[45]
$^0Tc_{Al,Fe:Va}^{BCC} = -437.95$ $^1Tc_{Al,Fe:Va}^{BCC} = -1719.7$	[52]
$L_{Al,Mn:Va}^{BCC} = -120077 + 52.851T + (y_{Al} - y_{Mn})(-40652 + 29.2764T)$	[46]
$L_{Fe,Mn:Va}^{BCC} = -2759 + 1.237T$	[47]
$^0Tc_{Fe,Mn:Va}^{BCC} = 123$	[47]
$L_{Fe,Mn:C}^{BCC} = 34052 - 23.467T$	[44]
$FCC : (Fe, Mn, Al)_1(C, Va)_1$	
$^0G_{Al:C}^{BCC} =^0 G_{Al}^{FCC} +^0 G_C^{graphite} + 81000$	[48]
$L_{Al:C,Va}^{FCC} = -80000 + 8T$	[48]
$L_{Fe:C,Va}^{FCC} = -34671$	[42]
$L_{Mn:C,Va}^{FCC} = -43433$	[44]
$L_{Al,Fe:Va}^{FCC} = -104700 + 30.65T + (y_{Al} - y_{Fe})22600 + (y_{Al} - y_{Fe})^2(29100 - 13T)$	[48]
$L_{Al,Mn:Va}^{FCC} = -69300 + 25T + (y_{Al} - y_{Mn})8800$	[46]
$L_{Fe,Mn:Va}^{FCC} = -7762 + 3.865T + (y_{Fe} - y_{Mn})(-259)$	[47]
$^0Tc_{Fe,Mn:Va}^{FCC} = -2282$ $^1Tc_{Fe,Mn:Va}^{FCC} = -2068$	[47]
$L_{Al,Fe:C}^{FCC} = -104000 + 80T + (y_{Al} - y_{Fe})81000$	[48]
$L_{Fe,Mn:C}^{FCC} = 34052 - 23.46T$	[47]
$L_{Al,Fe,Mn:Va}^{FCC} = 0$	[53]
$L_{Al,Mn:C,Va}^{FCC} = 50000$	[53]
$L_{Al,Fe,Mn:C}^{FCC} = -679200 + 400T$	[53]
$\kappa - carbide : (Fe, Mn)_3Al_1(C, Va)_1$	
$^0G_{Fe:Al:C}^{\kappa} = 3^0G_{Fe}^{FCC} +^0 G_{Al}^{FCC} +^0 G_C^{graphite} - 115000 + 25.2T$	[53]
$^0G_{Mn:Al:C}^{\kappa} = 3^0G_{Mn}^{FCC} +^0 G_{Al}^{FCC} +^0 G_C^{graphite} - 150920 + 40T$	[53]
$^0G_{Fe:Al:Va}^{\kappa} = 3^0G_{Fe}^{FCC} +^0 G_{Al}^{FCC} - 94000 + 17.6T$	[53]
$^0G_{Mn:Al:Va}^{\kappa} = 3^0G_{Mn}^{FCC} +^0 G_{Al}^{FCC}$	[53]
$L_{Fe,Mn:Al:C}^{\kappa} = 9600$	[53]
$L_{Fe:Al:C,Va}^{\kappa} = 13752 - 24T$	[53]

Yao et al. demonstarted by an atom probe study that the partitioning behaviour of κ-carbide greatly depends on the alloying element [32]. Therefore, the order parameter of simple cubic sublattices was expressed by the site fraction in each sublattice according to Landau-Lifshitz's rule [54, 55, 56]. The order parameters and the concentrations for Mn, Al, and C were expressed as:

6

$$\phi_i^1 = \frac{(2y_i^{(1)} - y_i^{(2)} - y_i^{(3)})}{3c_i} \quad i = Mn, Al, (C, Va) \tag{5a}$$

$$\phi_i^2 = \frac{(y_i^{(1)} - 2y_i^{(2)} + y_i^{(3)})}{3c_i} \quad i = Mn, Al, (C, Va) \tag{5b}$$

$$\phi_i^3 = \frac{(y_i^{(1)} + y_i^{(2)} - 2y_i^{(3)})}{3c_i} \quad i = Mn, Al, (C, Va) \tag{5c}$$

$$c_i = \frac{(y_i^{(1)} + y_i^{(2)} + y_i^{(3)})}{3} \quad i = Mn, Al, (C, Va) \tag{5d}$$

In this way, each site fraction $y_i^{(s)}$ can be rewritten as function of order parameters ϕ_i^s. Eq.5d only holds when Fe atoms are exchanged with Mn atoms. For Fe, we have:

$$c_{Fe} = 1 - \sum_i c_i \tag{6a}$$

$$y_{Fe}^{(s)} = 1 - \sum_i y_i^{(s)} \tag{6b}$$

where $\phi_{Al}^i (i = 1, 2, 3)$, $\phi_{Mn}^i (i = 1, 2, 3)$, $\phi_{C,Va}^i (i = 1, 2, 3)$, and c_{Al}, c_{Mn}, $c_{C,Va}$ refer to the order parameter and the composition fields of Al, Mn, and (C, Va), respectively. By combining equation 1 - 6, the molar Gibbs energy of the disordered and ordered phases for the quaternary Fe-Mn-Al-C system can be described with the variables of the order parameter and composition fields for elements. The total free energy $F^{quaternary\ system}$ in the Fe-Mn-Al-C system included the local free energy density, the interface energy and strain energy, was given by:

$$F^{quaternary\ system} \equiv \int_V (\frac{1}{V_m} G^{disord\ or\ L1_2} + \frac{\alpha}{2} \sum_{i=Mn,Al,(C,Va)}^{3} (\nabla c_i)^2$$

$$+ [\frac{\beta}{2} \sum_{i=Mn,Al,(C,Va)}^{3} (\nabla \phi_i^j)^2] + g_V^{el}) dV \tag{7}$$

where V_m is the molar volume which is considered to be constant. α and β are the

gradient energy coefficients for the compositions and order parameters, respectively. Interfacial anisotropy introduced into phase-field model by making interface energy (σ) orientation-dependant by [38]:

$$\sigma(\hat{n}) = \frac{1.1}{d\lambda}\beta(\hat{n})^2 \tag{8}$$

The gradient energy coefficient is expressed as:

$$\beta(\hat{n}) = \beta_0 + \beta_1(n_x^2 + n_y^2 + n_z^2 + n_x^2 + n_x^2 + n_y^2 n_z^2 + n_x^2) + \beta^2 n_x^2 n_y^2 n_z^2$$
$$+ \beta_3(n_x^2 + n_y^2 + n_z^2 + n_x^2 + n_x^2 + n_y^2 n_z^2 + n_x^2)^2 \tag{9}$$

where n_x, n_y and n_z are Cartesian coordinates of the normal to the interface. $\beta_0 = \lambda_0\sqrt{k_0}$, $\beta_1 = \frac{\lambda_0 k_1}{2\sqrt{k_0}}$, $\beta_2 = \frac{\lambda_0 k_2}{2\sqrt{k_0}}$ and $\beta_3 = \frac{\lambda_0 k_3}{2\sqrt{k_0}} - \frac{\lambda_0 k_1^2}{8k_0\sqrt{k_0}}$, where $\lambda_0 = \sqrt{3\lambda/1.1}$. This expression is different from the expansion based on cubic harmonics [62]. An example is that the leading anisotropic term is not $(n_x^4 + n_y^4 + n_z^4)$ but $(n_x^2 + n_y^2 + n_z^2 + n_x^2 + n_x^2 + n_y^2 n_z^2 + n_x^2)$.The values of anisotropy coefficients k_i are listed in Table. 2. The interface normal vector in the phase-field model was computed by $\hat{n} = \frac{\nabla\phi}{|\nabla\phi|}$.

Table 2: Anisotropy coefficients used in the present work. The united for coefficients are in erg/cm^2 [38].

Coefficient	k_0	k_1	k_2	k_3
Values	2258.53	-3291.47	12959.9	1880.74

The morphology of κ-carbide is directly related to the coherency between matrix and precipitates [29]. κ-carbide and austenite have a strong coherency because of the similar lattice parameter and crystal structure. Cube to cube orientation relationship between κ-carbide and austenite is repeatedly reported [30]. Therefore, precipitation of fine κ-carbides is possible in austenite. Besides, κ-carbide has well-known Nishiyama-Wasserman relationship ($(110)_\alpha||(111)_{\kappa-carbide}, [001]_\alpha||[10\bar{1}]_{\kappa-carbide}$) with ferrite matrix [31]. Experimental observations show that κ-carbides precipitated in ferrite matrix are coarse and because of the semi-coherency between two phases. In this study, the contribution of elastic strain energy was, hence, taken into account in order to sim-

ulate more realistic morphology. Cube to cube and Nishiyama-Wasserman orientation relationships were considered between κ-carbide and γ and α, respectively. In Eq. 7, G_V^{el} represent the elastic energy density. Based on linear elasticity, the elastic strain energy is expressed as [57]:

$$G_V^{el} = \frac{1}{2}\int_V \sigma_{ij}\epsilon_{ij}^{el}dV = \frac{1}{2}\int_V C_{ij}\epsilon_{ji}^{el}\epsilon_{ij}^{el}dV \tag{10}$$

where C_{ij} is the tensor of elastic constants. the values of elastic constants are presented in Table.3. The elastic strain is defined as the difference between the actual strain, $\epsilon_{ij}^{act}(\overrightarrow{r})$, and the stress-free strain, $\epsilon_{ij}^{0}(\overrightarrow{r})$:

$$\epsilon_{ij}^{el}(\overrightarrow{r}) = \epsilon_{ij}^{act}(\overrightarrow{r}) - \epsilon_{ij}^{0}(\overrightarrow{r}) = \frac{1}{2}\left(\frac{\partial u_i(\overrightarrow{r})}{\partial r_j} + \frac{\partial u_j(\overrightarrow{r})}{\partial r_i}\right) - p(\phi)\epsilon_{ij}^{00} \tag{11}$$

where ϵ_{ij}^{00} denotes the eigenstrain corresponding to the precipitate of the κ-carbide. Eigenstrain, also known as stress-free transformation strain (SFTS), represents the strain that takes place inside the material when the external constraints are absent during phase transformations. $p(\phi_i^j) = (\phi_i^j)^3(6(\phi_i^j)^2 - 15(\phi_i^j) + 10)$ is the interpolation function. The physical parameters used for calculations are presented in Table. 4.

Table 3: Bulk modulus and Elastic constants of various forms of κ-carbide, α-iron and γ-iron in GPa. Cubic crystals have only three independent constants, C_{11}, C_{12} and C_{44} and tetragonal structures have additional three constants C_{13}, C_{33} and C_{66}. The values for κ-carbide are taken from Ref.[58]. The values for α-Fe are taken from Ref.[59]. The values for γ-Fe are taken from Ref.[60].

	B_0	C_{11}	C_{22}	C_{44}	C_{13}	C_{33}	C_{66}
Fe_3Al	168	185	160	124	-	-	-
Fe_3AlC	203	426	91	65	-	-	-
Fe_2MnAlC	202	422	74	92	92	463	92
$FeMn_2Al$	234	465	86	96	138	455	100
Fe_3Al	218	454	100	106	-	-	-
α-Fe	167	200	135	117	-	-	-
γ-Fe	152	230	129	125	-	-	-

Table 4: Physical parameters used in this model.

Description	Parameter	Value
Lattice parameter for γ	a_γ	3.54 ($\mathring{A}$) [64]
Lattice parameter for α	a_α	2.92 ($\mathring{A}$) [64]
Lattice parameter for κ	a_κ	3.85 ($\mathring{A}$) [63]

The mechanical equilibrium condition can be given by:

$$\frac{\partial \sigma_{ij}(r)}{\partial r_j} = 0 \tag{12}$$

The evolution equation was linked to the mechanical equilibrium equations to find the displacement u_i:

$$C_{ijkl}[\frac{1}{2}(u_{k,lj} + u_{l,kj}) - \epsilon_{kl}^{00} \frac{\partial}{\partial r_j}(p(\phi))] = 0 \tag{13}$$

The SFTS was determined by the orientation relationship between κ phase and γ and α phases. Small strain tensor e for one κ-carbide was determined according to the orientation relationships and the finite-strain approximation $\epsilon_i^{00}j - \frac{1}{2}(e + e^T + eTe)$ was, then, used to determine the SFTS tensor. The temporal evolution of the elemental concentrations and order parameters can be determined by calculating the following non-linear Cahn-Hilliard diffusion equations and time-dependant Ginzburg-Landau equations:

$$\frac{\partial c_i}{\partial t} = \sum_j \nabla.(\tilde{M}_{ij} \nabla \frac{\delta F}{\delta c_j}), \quad i = Mn, Al, (C, Va), \quad j = Mn, Al, (C, Va) \tag{14}$$

$$\frac{\partial \phi_i^j}{\partial t} = -L\frac{\delta F}{\delta \phi_i^j}, \quad i = Mn, Al, (C, Va), \quad j = 1, 2, 3 \tag{15}$$

where $\tilde{M}_{ij}$ and L are the diffusion mobility and the structural relaxation, respectively. The diffusion mobility, $\tilde{M}_{ij}$, was expressed by the atomic mobilities of Mn, Al, C and Fe using the following equation:

$$\tilde{M}_{ij} = \sum_n (\delta_{in} - c_i)(\delta_{jn} - c_j)c_n M_n^{Fe} \tag{16}$$

where δ_{in} and δ_{jn} represent the Kronecker delta. From the absolute-reaction rate theory arguments, the atomic mobility may be divided into a frequency of factor M_B^0

10

and an activation enthalpy Q_B and is given by:

$$M_B = exp(\frac{RTlnM_B^0}{RT})exp(\frac{-Q_B}{RT})\frac{1}{RT} \qquad (17)$$

The composition dependence of Φ_B which represents $RTlnM_B^0 - Q_B$ can be expressed by the Redlich-Kister expansion in the form of CALPHAD approach [69] and is given in Table.5. The use of CALPHAD formalism for the expression of mobilities makes it possible to simulate the evolution of κ phase at various temperatures.

Table 5: Summary of atomic mobilities of Al, Mn and C used in the present work (all in SI units).

Parameter	Value	Refs.
Φ_{Al}^{Fe}	$RTln(6.5 \times 10^{-5})$	[70]
Φ_{Mn}^{Fe}	-246512.70-104.56T	[71]
Φ_C^{Fe}	-148123.29-88.33T	[71]

The kinetic parameter L is considered to be related to the diffusional mobility of carbon M_C^{Fe} as following: $L = c_C y_{Va} M_C^{Fe}$ where y_{Va} is the fraction of vacant interstitials, i.e. $(1 - c_C/3)$ for α and $(1 - c_C)$ for γ. Parameter L for κ was assumed to obey the following relationship $\tilde{M}_{CC} = La_0/16$ [40] with the lattice parameter $a_0 = 3.85 \times 10^{-10}$ m. Gradient energy coefficient was chosen to be $\alpha = 1.56 \times 10^{-14} Jm^2/mol$. This value observed using atom probe analysis and the cluster variation method for multicomponent systems [61]. In this study the interface was defined in the region between $\phi = 0.1$ and $\phi = 0.9$. At the nucleation stage for single particle simulation, a small cube with a side of $3\sqrt{2}$ nm in the field were transformed to κ-carbide phase. For multi-particle simulations, the number of nucleus in the field was determined according to experimental observations reported in Ref.[14, 31]. The mole fractions were set as Al=0.145, Mn=0.198 and C=0.081. The values of order parameters were also set as Al=o.676, Mn=0.738 and C=0.305. A semi-Implicit-Fourier-Spectral-Method [66] was employed for numerical analysis with a periodical boundary condition. The system size for the simulation is $300\Delta x \times 300\Delta x \times 300\Delta x$ (grid size: $\Delta x = 0.25nm$) for 3D single particle simulations and $1000\Delta x \times 1000\Delta x \times 1000\Delta x$ for 3D multi-particle simulations. This

method is programmed in C++ and the output is visualized using an in-house visual-ization software (ARVisual) developed in our research group.

3. Results and discussion

It is well-known that the morphological evolution of precipitates is mainly de-termined by the interaction between the elastic strain energy and interfacial energy. Thus, these energetic contributions were taken into account in the present phase-field model,Eq. 7, to quantitatively determine the κ-carbide morphology evolution in both γ and α phases. The investigation began by simulating a single κ precipitate in both disordered FCC (γ) and BCC (α) phases.

The interfacial and elastic strain energies have different effects on the morphology of κ precipitates. As reported in the literature, the coherency between κ-carbide with γ matrix is different from that between κ-carbide and α matrix [31]. This difference in coherency, in turn, results in different precipitate morphologies in γ and α phases. A number of controlled phase-field simulations for a single κ precipitate were carried out to investigate the effects of both energetic contributions. In these simulations, a cuboidal nucleus with a side of $3\sqrt{2}$ nm was manually transformed to κ in the centre of the system.

A number of cases were investigated in these simulations to study the effect of each contributing energy. In the first scenario, the interfacial energy was only assumed to be the contributing energy. Secondly, the contribution of elastic energy to the precipitate's morphology was studied, with interfacial energy of $10\ mJm^{-2}$. Finally, the contribu-tion of both energies were investigated. To explain each energetic contribution, total elastic strain energy E_{el} and total interfacial energy E_{int} throughout the simulation domain were determined (Fig. 3). The length of κ precipitates along the [100], [010] and [001] directions were, also, calculated in both diordered phases to compare the precipitate's size when formed in different matrix.

The simulation results for a single κ precipitate are presented in Fig. 1a - 1b. As shown in Fig.1, κ-carbide contain two main morphologies, namely, {001} faceted cuboidal in austenite (Fig. 1a) and elongated plate-like aligned the elastically soft

12

< 100 >-type directions (Fig. 1b). These series of simulation demonstrated the interaction between interfacial and elastic strain energies as well as their relative values. As shown in Fig. 2a, assuming the contribution of interfacial energy only (blue), the $L_{[100]}/L_{[010]}$ aspect ratio for γ matrix remained constant as the precipitate has a cuboidal shape in this phase, while in α phase, it increased slightly from the starting value and reached a plateau with a value close to 1.3. In the second scenario where the elastic strain energy was considered while the evolution of interfacial was ignored (red), strain energy increased to a critical value close to 1.1 for a κ-carbide formed in γ and remained unchanged for the rest of simulation time. A continuous increase in the $L_{[100]}/L_{[010]}$ aspect ratio was observed when the precipitate formed in α. Because of the high lattice mismatch, the elastic strain energy was the dominant mechanism in determining the morphology of the precipitates in α phase, as can be seen in Fig 2b. That is the reason for the elongated plate-like κ-carbide in α phase.

Fig. 3 shows the ratio of total elastic strain energy (E_{el}) to total interfacial energy (E_{int}) in α matrix. When the contribution of both energies was taken into account, as it was expected the morphological change of κ was controlled by the interfacial energy at the early stages of precipitation while the elastic strain energy became dominant at the later stages as indicated by black line in Fig. 3. The minimization of interfacial energy, thus, dominates the precipitates morphology in both γ and α phases at initial stages of precipitation. As the precipitate grows, the minimization of elastic strain energy dominates the precipitate morphology, and the $L_{[100]/L_{[010]}}$ aspect ratio will again exceed the critical value close to 1.8, even faster than when elastic energy was only considered. During the growth process, elastic strain energy exists throughout the precipitate whereas interfacial energy only contributes to the γ/κ or α/κ interfaces. The significant change in the morphology of κ when formed in α compared to that when precipitates in γ is the direct manifestation of high degree of misfit between κ particle and the α matrix (between γ and κ this value is about 1.88% and between α and κ this value is about 5.8%) [31].

Obviously, the total interfacial energy (E_{int}) is larger than the total elastic strain energy of the system when the precipitate is small, due to the fact that the area to volume ratio of the precipitate is high. As κ continues to grow, the area to volume ratio

13

reduces and the contribution of elastic energy to the morphology of precipitate becomes dominant. The morphological evolution of κ precipitate can be, hence, elucidated as a direct effect of the two competing energetic contributions during the growth process.
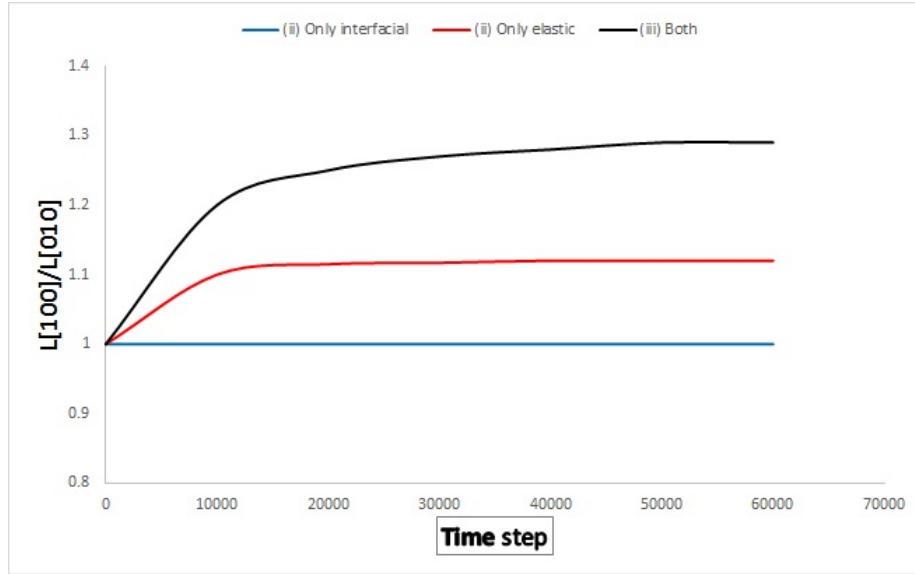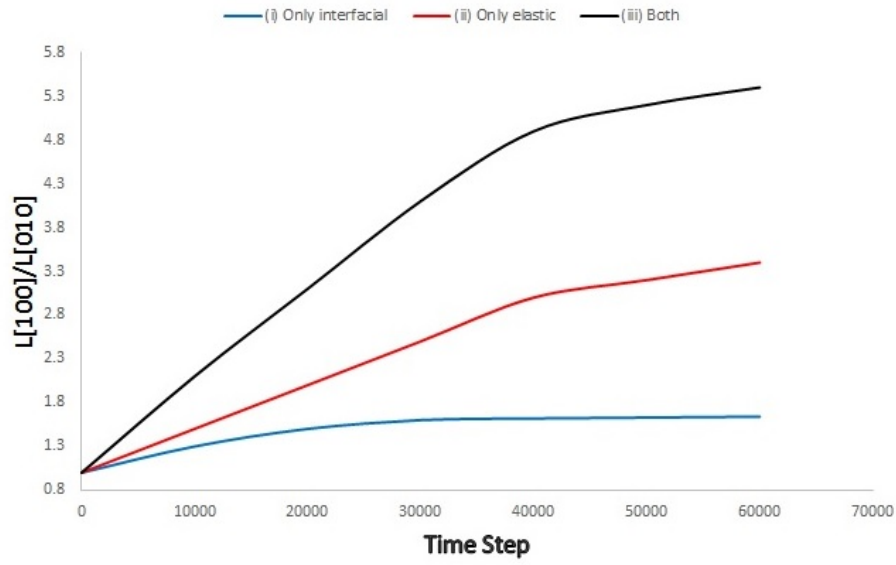
14
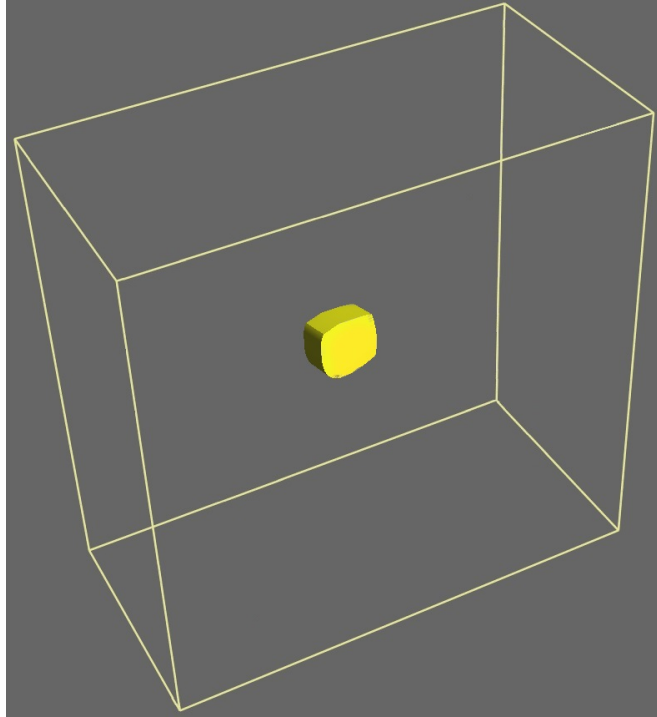
(a)
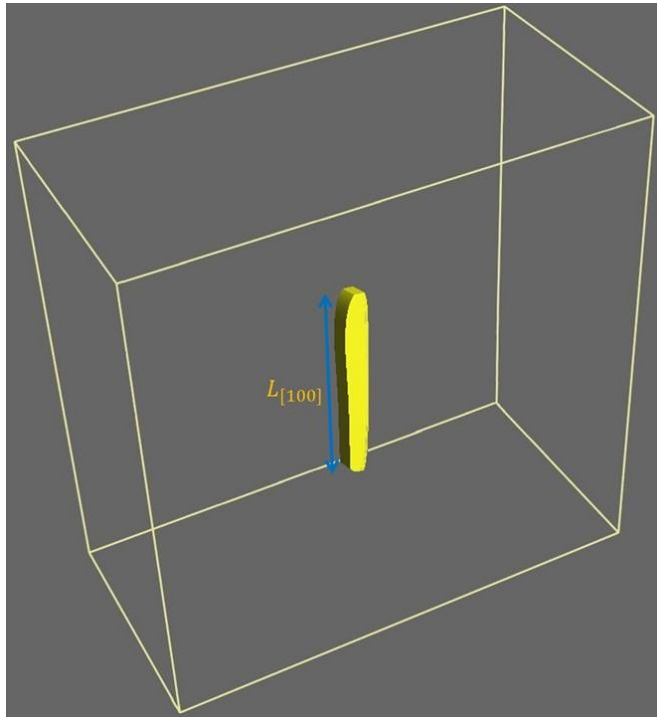
(b)

15

Figure 1: The morphology of a single κ-carbide in a) γ phase and b) α phase at $t^* = 60,000\Delta t$.

(a)

(b)

Figure 2: Evolution of $L_{[100]}/L_{[010]}$ aspect ratio of κ-carbide precipitate under different conditions: a) in a γ grain and b) in an α grain.

The phase-field simulation also shed light on the synergetic effects of both con-tributing energies on increasing the $L_{[100]}/L_{[010]}$ aspect ratio when the formation of

16

κ-carbide was simulated in α phase. The SFTS ratio along the $[100]_\kappa$ and $[010]_\kappa$ directions was calculated to be 0.116 implying that the system tends to minimize its total elastic strain energy by favouring a higher $L_{[100]}/L_{[010]}$ ratio. Moreover, the ratio of interfacial energy $\sigma_{(100)}/\sigma_{(010)}$ was determined to be 1.1, indicating that the minimization of interfacial energy was taken place on the (010) and (100) plane areas, which is equivalent to increasing the $L_{[100]}/L_{[010]}$ ratio. Hence, both contributing energies, namely interfacial and elastic strain energies, tend to increase the aspect ratio of $L_{[100]}/L_{[010]}$ when κ-carbide precipitates growing in the α matrix.
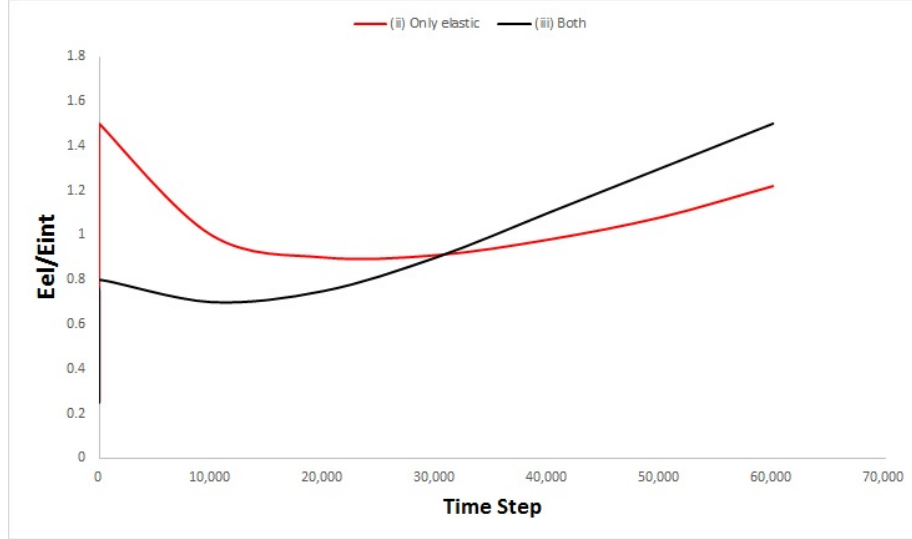

Figure 3: Evolution of ratio of total elastic strain energy to total interfacial energy under different conditions.

Fig. 4 and 5, show the multi-particle simulations of κ phase in γ (Fig. 4) and in α (Fig. 5). In the γ phase, κ has a cuboidal morphology with rounded corner which is in agreement with what reported in Ref. [67], while it consists of elongated plate-like morphology in the α phase. The simulated particles' morphology in ferrite agrees with TEM observations reported in Ref.[31]. Phase-field simulation revealed that the interparticle spacing between cuboids is around $20\Delta x$ while this value increases to $90\Delta x$ in α phase. Due to morphology and interparticle spacing, κ-carbides form stronger obstacles in γ phase than α phase and thus can lead to dislocation-particle pining events more effective strengthening mechanism in γ.
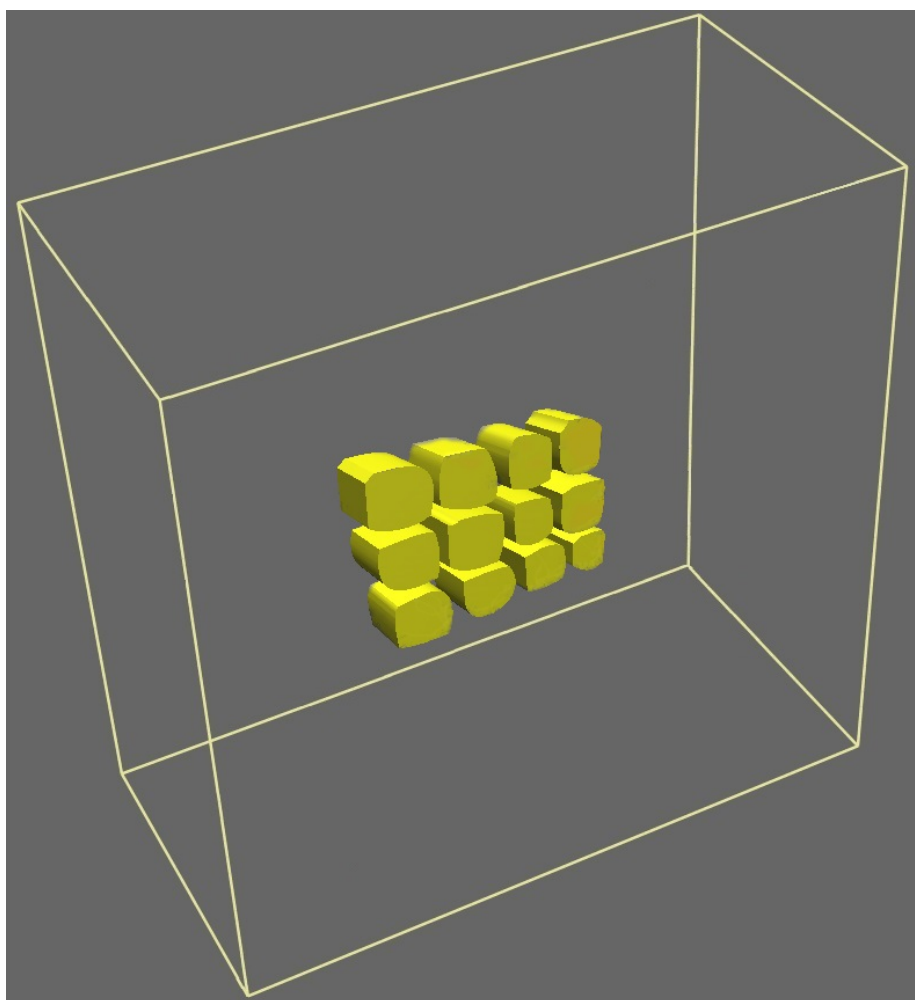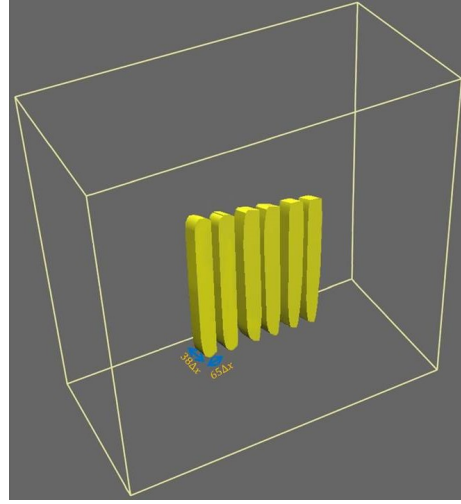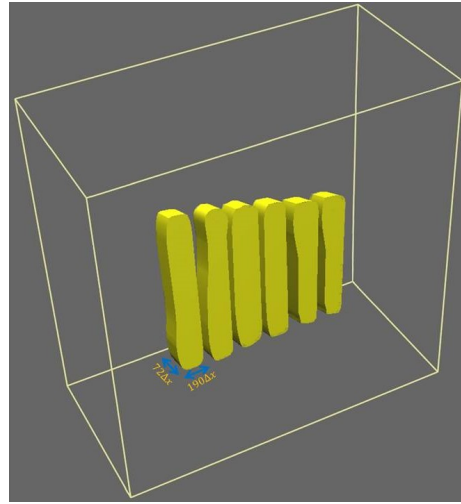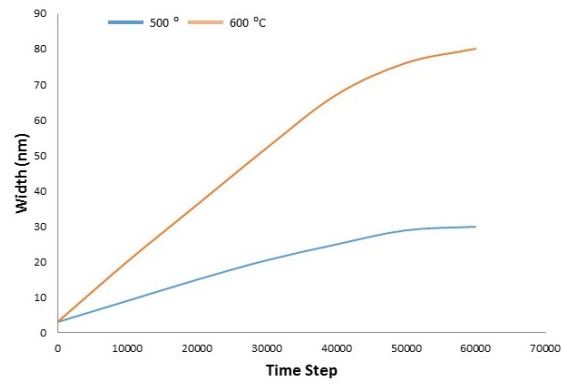
17

Figure 4: Morphology and size of κ-carbide in γ matrix.

(a)

(b)

(c)

19

Figure 5: Simulation of κ-carbide precipitates at two different isothermal holding temperature: a) at $500^\circ C$ b) at $600^\circ C$, c) the evolution of precipitate's average width at $500^\circ C$ (blue) and $600^\circ C$ (red) for $t^* = 60,000\Delta t$.

We carried out two specific phase-field simulations for the growth of κ precipitate in a ferritic steel with a composition 1.2 C, 3.2 Mn and 10 Al (at .%) for two different annealing temperatures, namely, $500^\circ C$ and $600^\circ C$ in order to investigate the effect of holding temperature on the morphology of κ phase in α. The simulation results are shown in Fig. 5a and Fig.5b for the microstructure evolution at $500^\circ C$ and $600^\circ C$, respectively. Fig. 5c shows the evolution of the precipitate's average width with computation time. The width of κ-particles increased with a higher annealing temperature. The average width of κ formed at $500^\circ C$ evolved much more slower than that of κ-carbides formed at $600^\circ C$. After $t^* = 60,000\Delta t$, the average widths of κ-particles at 500 and $600^\circ C$ are 16.25 and 47.5 nm respectively, as shown in Table.6. During isothermal holding at $500^\circ C$, a larger driving force for the κ-carbide precipitation exists. The morphological evolution of κ-particles for different isothermal holding temperatures is due to the fact that during isothermal annealing at $500^\circ C$ the γ decomposition kinetics into κ phase is retarded due to the lower diffusion rate of solutes, especially C, compared to the simulation carried at $600^\circ C$. Thus, the κ-carbides formed at $500^\circ C$ show a finer distribution compared to that formed at $600^\circ C$. During the growth process, it is the diffusion of C during annealing treatment that primarily controls the morphology of κ particles.

Table 6: Comparison between simulation results and experimental values.

Description	simulation		experiment	
Isothermal temperature	$500^\circ C$	$600^\circ C$	$500^\circ C$	$600^\circ C$
Width (nm)	16.25	47.5	17	45

4. Conclusion

We developed a phase-field method which coupled to CALPHAD in order to simulate the evolution of ordered κ-carbide in both disordered α and γ phases. CALPHAD formalism was employed in the present work in order to simulate a realistic complex morphology evolution in a multicomponent Fe-C-Mn-Al system. A three-sublattice model was used to allow intermixing between Fe and substitutional Mn atoms on the cube face site and incomplete filling of C atoms in the central octahedral site of the

ordered structure. This study demonstrated the usefulness of phase-field method coupled to CALPHAD for predicting the microstructure morphology, showing governing factors and further providing guidance for material design. The Results demonstrate that κ consists of cuboids with rounded corners in γ and elongated plate-like in α. The volumetric E_{el} and E_{int} are calculated in the present study showing that interfacial energy dominates the particles' morphology at initial stages of precipitation, while at later stages, it is the elastic strain energy that controls the morphological evolution. The channels between particles in γ is in overall much more narrower than that in α. This means that κ can be considered as more effective strengthening mechanism in austenite. Simulations were performed for two different isothermal holding temperature in order to explore the change in κ phase shape in α with alteration of temperature. In general, increasing the holding temperature leads to a remarkable increase in the size of the κ carbides.

Acknowledgement

References

[1] Mayyasa A, Qattawia A, Omara M, Shan D. Renew Sustain Energy Rev 2012; 16:1845-62.

[2] Kuziak R, Kawalla R, Waengler S. Arch. Civ. Mech Eng 2008; 8:103-17.

[3] Matlock DK, Speer JG, Third generation of AHSS: microstructure design concepts, in: Halder A, Suwas S, Bhattacharjee SD (Eds), Mcirostructure and Texture in Steels and other Materials, springer, London, 2009, 185-205.

[4] Ma M, Yi H. Lightweight car body and application of high strength steels, in: Weng Y, Dong H, Gan Y (Eds), Advanced Steels, Springer, Berlin Heidelberg, Heidelberg, 2011, 187-198.

[5] Rana R, Liu C, Ray RK. Scr. Mater. 2013;68:354-9.

[6] Sohn SS, Lee BJ, Lee S, Kim NJ, Kwak JH. Acta Mater 2013; 61:5050-66.

[7] Sohn SS, Song H, Suh BC, Kwak JH, Lee BJ, Kim NJ, Lee S, Acta Mater 2015; 96:301-310.

[8] Frommeyer G, Brux U, Steel Res. Int. 2006; 77:627-33.

[9] Lilly AC, Deevi SC, Gibbs ZP. Mater. Sci. Eng. A 1998; 258:42-9.

[10] Choo WK, Kim JH, Yoon JC. Acta Mater. 1997; 45:4877-4885.

[11] Hwang SW, Ji JH, Lee EG, Park KT, Mater. Sci. Eng. A 2011; 528:5196-5203.

[12] Sahraoui T, Hadji M, Yahi M. Mater. Sci. Eng. A 2009; 523: 271-6.

[13] Choi K, Seo CH, Lee H, Kim SK, Kwak JH, Chin KG, Park KT, Kim NJ. Scr. Mater. 2010; 63:1028-31.

[14] Gutierrez-Urrutia I, Raabe D. Scr. Mater. 2013; 68:343-47.

[15] Chen R, Xu Q, Liu B, comp. Mater.Sci. 2015; 105:90-100.

[16] Rahnama A, Qin RS. Comp. Mater.Sci 2015; 96:102-107.

[17] Rahnama A, Qin RS. Proc. ICME 2015, John Wiley & Sons, Inc. 147-154.

[18] Lin CL, Chao CG, Juang JY, Yang JM, Liu TF. J. All. Comp. 2014; 586:616-20.

[19] Xu T, Sarkar S, Wang Y. Acta Mater. 2012; 60:4787-99.

[20] Jamshidian M, Zi g, Rabczuk T. Comput. Mater. Sci. 2014; 95:663-71.

[21] Militzer M. Curr. Opin. Solid State Mater. Sci. 2011; 15:106-15.

[22] Lu Y, Zhang L, Chen Y, Chen Z, Wang Y. Intermetallics 2013; 38:144-9.

[23] Grafe U, Bottger B, Tiaden J, Fries SG. Scr. Mater. 2000; 42:1179-86.

[24] Fattebert JL, Wickett ME, Turchi PEA. Acta Mater. 2014; 62:89-104.

22

[25] Diego N.D, Plazaola F, Jimenez JA, Serna J, del Rio J. Acta Mater. 2005; 53:163-72.

[26] Lu Y, Lu G, Liu F, Chen Z, Tang K. J. Al. and Comp. 2015; 637:149-54.

[27] Zhang M, Wang Y, Chen Z. Proc. Eng. 2012; 27:1671-8.

[28] Hou H, Zhao Y, Zhao Y. Mater. Sci. Eng A 2009; 499:204-7.

[29] Heo YU, App. Mic. 2014; 44:144-9.

[30] Lin C L, Chao C G, Bor H Y, and Liu T F. Mat. Trans 2010; 51: 1084-8.

[31] Seol JB, Raabe D. Choi P, Park HS, Kwak JH, and Park CG, Scr. Mater. 2013;68:348-53.

[32] M.J. Yao, P. Day, J.-B Seol, P. Choi, M. Herbig, R.K.W. Marceau, T. Hickel, J. Neugebauer, D. Raabe, Acta Mater. 106 (2016) 229-238.

[33] M. Palm, G. Inden, Intermetallics 3 (1995) 443.

[34] K. Ishida, H. Ohtani, N. Satoh, R. Kainuma, T. Nishizawa, ISIJ Int. 30 (1990) 680.

[35] H. Ohtani, M. Yamano, M. Hasebe, ISIJ Int. 44 (2004) 1738.

[36] P. Villars, A. Prince, H. Okamoto (Eds.), Handbook of Ternary Alloy Phase Diagrams, ASM International, Materials park, OH, 1995, p. 2881.

[37] T. Kitashima, H. Harada. Acta Mater 57 (2008) 2020-2028.

[38] R.S. Qin, H.K.D.H. Bhadeshia, Acta Mater. 57 (2009) 2210-2216.

[39] T.T. Arif., R.S. Qin, Comp. Mater. Sci. 77 (2013) 230-235.

[40] Poduri R, Chen LQ. Acta Mater 46 (1998) 3915.

[41] J. Grbner, H.L. Lukas, F. Aldinger, J. Alloys Compd. 220 (1995) 8.

[42] P. Gustafson, Scand. J. Metall. 14 (1985) 259.

[43] P. Gustafson, An evaluation of the thermodynamic properties and the P, T phase diagram of carbon, Carbon 24 (1984) 169-176.

[44] W. Huang, Scand. J. Metall. 19 (1990) 26.

[45] M. Seiersten, SINTEF Report STF-28F93051, Oslo, Norway, 1993.

[46] A. Jansson, Metall. Trans. A 23A (1992) 2953.

[47] W. Huang, CALPHAD 13 (1989) 243.

[48] D. Conntable, J. Lacaze, P. Maugis, B. Sundman, CALPHAD 32 (2008) 361.

[49] N. Dupin, I. Ansara, B. Sundman, CALPHAD 25 (2001) 279-298.

[50] I. Ansara, N. Dupin, H.L. Lukas, B. Sundman, J. All. Comp. 247 (1997) 20-30.

[51] W. Huang, Metall. Trans. A 21A (1990) 2115.

[52] I. Ohnuma, Unpublished work, 2000.

[53] Chin KG, Lee HJ, Kwak JH, Kang JY, Lee BJ, J. All. Comp. 2010; 505:217-23.

[54] Zhu JZ, Wang T, Adrell AJ, Zhou SH, Liu ZK, Chen LQ. Acta Mater. 2004; 52:2873.

[55] Landau LD, Lifshitz EM. Statistical physics. London: Pergamon; 1980.

[56] Lai ZW. Phys Rev B 41 (1990) 9239.

[57] A. G. Khachaturyan, The Theory of Structural transformations in Solids, Wiley, New York, 1983.

[58] J.Y. Noh, H. Kim, J. Kor, Phys. Soc. 58 (2011) 285.

[59] S. A. Kim, W. L. Johnson, Mater. Sci. Eng. A 452-453 (2007), 633-639.

[60] K. Benyelloul, H. Aourag, Comp. Mater. Sci. 67 (2013) 353-358.

[61] Kitashima T, Yokokawa T, Yeh AC, Harada H. Intermetallics 2008;16:779.

[62] Karma A, Rappel WJ. Phys Rev E 1998;57:4323.

24

[63] Y.U. Heo, A Strategy for Phase Identification of Precipitates in High Al-containing Austenitic and Ferritic Steels Using Electron Diffraction, Applied Microscopy 44(4), (2014), pp. 144-149.

[64] J.D. Watson, P.G. McDougal, The crystallography of widmanstatten ferrite, Acta Matall. 21 (1973) 961-973.

[65] J. Agren, Computer simulations of the austenite/ferrite diffusional transformations in low alloyed steels, Acta Metall. 30 (1982) 841-851.

[66] Chen LQ, Shen Jie. Comput Phys Commun 1998; 108:147.

[67] Gutierrez-Urrutia, Raabe D. Scripta Mater 2013; 68: 343-347.

[68] J.O. Andersson, J. gren, J. Appl. Phys. 72 (1992) 1350-1355.

[69] J. gren, Current Opinion Solid. St, Mater. Sci. 1 (1996) 355-360.

[70] T. Helander, J. gren, Acta Mater. 47 (1999) 1141-1152.

[71] Y. Liu, L. Zhang, Y. Du, D. Yu, D. Liang, CALPHAD 33 (2009) 614-423.